Stable Boundary Layer Regimes in Single-Column Models

FELIPE D. COSTA,[a] OTÁVIO C. ACEVEDO,[b] LUIZ E. MEDEIROS,[a] RAFAEL MARONEZE,[a] FRANCIANO S. PUHALES,[b] ARLINDO D. CARVALHO JR.,[a] LUIS F. CAMPONOGARA,[a] DANIEL M. DOS SANTOS,[a] AND LUCA MORTARINI[c]

[a] *Universidade Federal do Pampa, Alegrete, Brazil*
[b] *Departamento de Física, Universidade Federal de Santa Maria, Santa Maria, Brazil*
[c] *Institute of Atmospheric Sciences and Climate, National Research Council, Bologna, Italy*

(Manuscript received 15 August 2019, in final form 27 March 2020)

ABSTRACT

Two contrasting flow regimes exist in the stable boundary layer (SBL), as evidenced from both observational and modeling studies. In general, numerical schemes such as those used in numerical weather prediction and climate models (NWPCs) reproduce a transition between SBL regimes. However, the characteristics of such a transition depend on the turbulence parameterizations and stability functions used to represent the eddy diffusivity in the models. The main goal of the present study is to detail how the two SBL regimes occur in single-column models (SCMs) by analyzing the SBL structure and its dependence on external parameters. Two different turbulence closure orders (first order and an E–l model) and two types of stability functions (short and long tail) are considered. The control exerted by the geostrophic wind and the surface cooling rate on the model SBL regimes is addressed. The model flow presents a three-layer structure: a fully turbulent, weakly stable layer (WSL) next to the surface; a very stable layer (VSL) above that; and a laminar layer above the other two and toward the domain top. It is shown that the WSL and VSL are related to both SBL regimes, respectively. Furthermore, the numerically simulated SBL presents the two-layer structure regardless of the turbulence parameterization order and stability function used. The models also reproduce other features reported in recent observational studies: an S-shaped dependence of the thermal gradient on the mean wind speed and an independence of the vertical gradient of friction velocity δu_* on the mean wind speed.

1. Introduction

The existence of two stable boundary layer (SBL) regimes has been firmly established in recent years from both observational and modeling studies (Mahrt et al. 1998; Sun et al. 2012; Van de Wiel et al. 2012a; Ansorge and Mellado 2014; Sun et al. 2015; van Hooijdonk et al. 2015; Acevedo et al. 2016; Baas et al. 2018; Lan et al. 2018, among others). Traditionally, since Mahrt et al. (1998) the SBL flow has been divided in two major regimes: a very stable boundary layer (VSBL), characterized by the presence of weak turbulence and large vertical gradients of mean quantities, and a weakly stable boundary layer (WSBL), where turbulence is much stronger than in the VSBL and the vertical gradients of mean quantities are reduced. Sun et al. (2012) showed that the VSBL–WSBL transition is locally controlled by the mean wind speed. However, the mean wind speed threshold for the transition is not universal, varying from one site to another (Acevedo et al. 2016; van Hooijdonk et al. 2015). In studies based on simplified numerical models (Van de Wiel et al. 2017; Holdsworth and Monahan 2019), it has been suggested that such differences may be associated to different surface characteristics, such as soil properties and the total surface net radiation.

Generally, the existence of two contrasting SBL regimes is reproduced by numerical schemes used to represent the interactions between the surface and the SBL (McNider et al. 1995; Derbyshire 1999; Acevedo et al. 2012; Ansorge and Mellado 2014; He and Basu 2015; Maroneze et al. 2019b). Using a simplified two-layer model, McNider et al. (1995), showed that the SBL regime is highly dependent on the initial conditions. Such a simplified model, however, is only capable of reproducing a nonturbulent or a fully turbulent regime, and this feature may be observed in weather numerical

Corresponding author: Felipe D. Costa, fdenardin@unipampa.edu.br

DOI: 10.1175/JAS-D-19-0218.1

prediction models as well (Derbyshire 1999). Shi et al. (2005) demonstrated that a very stable regime where the atmospheric levels are vertically decoupled from each other arises naturally in Reynolds-averaged Navier–Stokes (RANS) models of the SBL, regardless of the domain size and number of vertical levels considered, and these results have been later confirmed by McNider et al. (2012) using a complete single-column model. Both Derbyshire (1999) and Ansorge and Mellado (2014) have raised the important question whether such decoupling in the models is only a feature of the system of equations or also the simulation of a genuine feature of the SBL. This issue has been addressed by Maroneze et al. (2019b), who explored how simplified models reproduce differently the two SBL regimes as the variables being solved by prognostic equations, rather than parameterized, vary. Their results showed that a VSBL is simulated as long as the buoyancy effects are considered. Moreover, the VSBL regime is more realistically simulated when a prognostic equation for the turbulent heat flux is considered and better yet when temperature variance is also solved. In those cases, the relationship between turbulent kinetic energy and mean wind speed are contrastingly different between the two regimes, in a manner similar to what has been reported in the field (Sun et al. 2012, 2015). These results, therefore, indicate that the models and observations are indeed describing the same phenomenon. However, it is important to notice that the VSBL solved by low-order schemes that parameterize the heat flux present limitations that depend on the choice of parameterization.

Turbulence parameterizations are essential to describe the eddy diffusivity in air quality (McNider et al. 2018), numerical weather prediction (Savijärvi 2009; Steeneveld et al. 2010; Battisti et al. 2017), and climate models (Steeneveld et al. 2011; McNider et al. 2012). Among the models, the parameterizations may vary in regard to the order of turbulence closure or to how turbulent diffusivity is affected by the atmospheric stability (Cuxart et al. 2006). Generally, the influence of atmospheric stability is prescribed by an arbitrary stability function. Stability functions are mainly divided in two classes: short-tail (ST) stability functions, which suppress the mixing for intense stratification or long-tail (LT) stability functions that allow some finite mixing even under very strong stratification. Sandu et al. (2013) showed, using a climate model, that ST stability functions better represent the qualitative features of the boundary layer. Nevertheless, these models need some level of mixing to avoid an excessive cold bias near the surface and an impairment on the representation of large-scale processes, although Savijärvi (2009) and McNider et al. (2018) have indicated that this is dependent on model resolution. Baas et al. (2018) suggested that the problems pointed by Sandu et al. (2013) may be related with other physical process of the model, such as the coupling between the surface and the lower SBL, as they showed that both types of parameterizations are able to reproduce both SBL regimes and the transitions between them.

The main goal of the present study is to detail how the two SBL regimes occur in single-column models (SCMs) by analyzing the SBL structure and its dependence on external parameters. Contrasting with previous observational and modeling efforts, the SBL dynamics is analyzed as a whole, rather than at specific heights. By doing such, it is possible to verify whether different regimes occur simultaneously at different heights in the model. The two orders of closure (first order and an *E–l* model) and the two stability functions (ST and LT stability functions) used in the study are largely used in numerical weather prediction and climate models (NWPCs) around the world. Furthermore, it is verified how the SBL vertical structure is controlled by external parameters, such as the thermal and mechanical forcings, represented respectively by the geostrophic wind and surface cooling rate.

2. Model

For a flat surface and a dry atmosphere, neglecting the effects of advection and the radiative flux divergence, the equations governing the atmospheric flow in the planetary boundary layer can be written as follows:

$$\frac{\partial \overline{u}}{\partial t} = f(\overline{v} - \overline{v}_G) - \frac{\partial(\overline{u'w'})}{\partial z}, \tag{1}$$

$$\frac{\partial \overline{v}}{\partial t} = f(\overline{u}_G - \overline{u}) - \frac{\partial(\overline{v'w'})}{\partial z}, \tag{2}$$

$$\frac{\partial \overline{\theta}}{\partial t} = -\frac{\partial(\overline{w'\theta'})}{\partial z}, \tag{3}$$

where $\overline{u}$ and $\overline{v}$ are the wind components, $\overline{\theta}$ is the air temperature, f is the Coriolis parameter, $\overline{u}_G$ and $\overline{v}_G$ are the geostrophic wind components, $(\overline{u'w'})$ and $(\overline{v'w'})$ are momentum turbulent fluxes, and $(\overline{w'\theta'})$ is the turbulent sensible heat flux.

The turbulent fluxes are parameterized using K theory (Louis 1979; Therry and Lacarrère 1983; Delage 1997; Bélair et al. 1999; Weng and Taylor 2006; Cuxart et al. 2006, among others):

$$-(\overline{u'w'}) = K_M \frac{\partial \overline{u}}{\partial z}, \tag{4}$$

$$-(\overline{v'w'}) = K_M \frac{\partial \overline{v}}{\partial z}, \tag{5}$$

$$-(\overline{w'\theta'}) = K_H \frac{\partial \overline{\theta}}{\partial z}, \tag{6}$$

where K_M and K_H are the eddy diffusivity for momentum and heat, respectively. The two diffusivities are related to each other through the turbulent Prandtl number (Pr_t), as $K_H = K_M/\mathrm{Pr}_t$. In spite of the dependency of the turbulent Prandtl number on the atmospheric stability (Zilitinkevich et al. 2013; Li et al. 2015; Katul et al. 2014), for simplicity $\mathrm{Pr}_t = 0.85$ is used here.

a. Turbulence closure

The momentum and heat eddy diffusivities are necessary to determine the vertical turbulent fluxes in K theory. The order of the closure is defined according to Mellor and Yamada (1974). Generally, weather forecast or climate models use one of two possible parameterizations to evaluate the turbulent diffusivity in the boundary layer: first order or E–l schemes (Weng and Taylor 2003; Cuxart et al. 2006; Svensson et al. 2011).

1) FIRST-ORDER SCHEME

In the first-order models (hereinafter 1st), the eddy diffusivity is (Louis 1979)

$$K_M = l_m^2 \frac{\partial \overline{U}}{\partial z} f_m(\mathrm{Ri}), \tag{7}$$

where $\overline{U}$ is the mean wind speed and $f_m(\mathrm{Ri})$ is a stability function that depends on the local Richardson number (Ri):

$$\mathrm{Ri} = \frac{g}{\Theta} \frac{(\partial \overline{\theta}/\partial z)}{(\partial \overline{u}/\partial z)^2 + (\partial \overline{v}/\partial z)^2}. \tag{8}$$

For both types of closure presented in this work, the mixing length l_m has been evaluated following Blackadar (1962):

$$\frac{1}{l_m} = \frac{1}{\kappa z} + \frac{1}{\lambda_0}, \tag{9}$$

where κ is the von Kàrmàn constant and λ_0 is the mixing length for neutral flows (Delage 1974; Weng and Taylor 2003). Following Weng and Taylor (2006), $\lambda_0 = 40$ m is assumed.

2) E–l SCHEME

Using a third-order closure model, André et al. (1978) showed that a model based on a simple diffusion scheme cannot reproduce many features of the PBL diurnal cycle, as the schemes should be refined enough to distinguish and represent the diurnal and nocturnal period characteristics and forcings. Therry and Lacarrère (1983) used André et al. (1978) results to develop the K–E model, a 1.5-order closure model that evaluates the eddy diffusivity from the turbulent kinetic energy (TKE) budget equation. If an equation for the mixing length is included, the model is referred as the E–l model (Weng and Taylor 2003, 2006). In the E–l scheme the turbulent fluxes are still diagnostically evaluated form Eqs. (4)–(6), and the momentum eddy diffusivity is parameterized as

$$K_m = \sqrt{\alpha^{-1}\overline{e}}\, l_m f_m(\mathrm{Ri}), \tag{10}$$

where $\overline{e}$ is TKE, α is the ratio between the shear stress and TKE near the surface (Cuxart et al. 2006; Weng and Taylor 2006). Rodrigo and Anderson (2013) and Acevedo et al. (2014) have shown that the value of α is independent of height and it is also highly dependent on the flow stability. Here, it is assumed that $\alpha = 4(1 + 2.5z\Lambda^{-1})^{1/3}$, where Λ is the local Obukhov length (Acevedo et al. 2014).

As K_m depends on TKE, the E–l scheme has an additional equation for this variable (Therry and Lacarrère 1983; Weng and Taylor 2006; Cuxart et al. 2006; Bélair et al. 1999, among others):

$$\frac{\partial \overline{e}}{\partial t} = -\overline{u'w'}\frac{\partial u}{\partial z} - \overline{v'w'}\frac{\partial v}{\partial z} + \frac{g}{\Theta}\overline{w'\theta'} - \frac{\partial \overline{w'e'}}{\partial z} - \varepsilon. \tag{11}$$

In Eq. (11) g is the gravitational acceleration, Θ is the reference temperature, $(\overline{w'e'})$ is the turbulent flux of TKE, and ε is the TKE viscous dissipation. The transport term in Eq. (11) is written as

$$-\frac{\partial \overline{w'e'}}{\partial z} = \frac{\partial}{\partial z}\left(K_e \frac{\partial \overline{e}}{\partial z}\right), \tag{12}$$

where $K_e = K_M/\sigma_e$, and $\sigma_e = 1$ is the turbulent Prandtl number for TKE (Duynkerke 1988). The viscous dissipation is estimated by (Tikhomirov 2012; Therry and Lacarrère 1983)

$$\varepsilon = c_\varepsilon \frac{(\overline{e})^{3/2}}{l_d}. \tag{13}$$

The constant c_ε in Eq. (13) makes explicit the anisotropy in the SBL turbulent flow (Cuxart et al. 2006). Puhales et al. (2016) showed that it is not appropriate to use a fixed value for c_ε, because it depends strongly on the stability of the flow. Cuxart et al. (2006) stressed that the values of c_ε varied by an order of magnitude in the operational models compared in their study. Here, following Weng and Taylor (2003) we assume $c_\varepsilon = \alpha^{-3/2}$.

Finally, the mixing length for the viscous dissipation is assumed as $l_d = l_m$ (Therry and Lacarrère 1983; Weng and Taylor 2003; Cuxart et al. 2006; Weng and Taylor 2006, among others).

In this scheme, the effect of terms that do not affect the Richardson number, such as the turbulent transport of TKE or its dissipation rate, has been included in the turbulence formulation. In contrast, the previously described first-order closure, entirely based on the Richardson number, only takes in account the roles of turbulence shear production and buoyant destruction.

b. Stability functions

In both Eqs. (7) and (10) the atmospheric stability is parameterized as a function of Ri (Louis 1979; Zhang and Anthes 1982; Delage 1997; Holtslag and Boville 1993; Cuxart et al. 2006, i.a.). Weather forecasting and climate models use either ST or LT stability functions. An ST function assumes a critical value for Ri, beyond which turbulence in the flow is completely suppressed (McNider et al. 1995; Derbyshire 1999; Van de Wiel et al. 2002a). On the other hand, the LT stability functions allow the existence of turbulence even under very intense stratification (large Ri) (Louis 1979; Delage 1997; Poulos and Burns 2003).

Following England and McNider (1995) and McNider et al. (1995), a quadratic form for the ST stability function may be obtained from the Monin–Obukhov shear similarity functions (England and McNider 1995) and can be written as

$$f_m(\mathrm{Ri}) = \begin{cases} (1 - \mathrm{Ri}/\mathrm{Ri}_c)^2, & \text{for} \quad \mathrm{Ri} < \mathrm{Ri}_c \\ 0, & \text{for} \quad \mathrm{Ri} \geq \mathrm{Ri}_c \end{cases}. \tag{14}$$

Notice that, $f_m(\mathrm{Ri})$ vanishes when Ri is greater than $\mathrm{Ri}_c = 0.25$ (the critical Richardson number) and no mixing and no diffusion occur for $\mathrm{Ri} > \mathrm{Ri}_c$.

In favor of LT stability functions, Louis (1979) pointed out that the existence of some turbulence even in very stable conditions ($\mathrm{Ri} > \mathrm{Ri}_c$) in the models prevents the runaway cooling problem, when the air temperature near the surface keeps decreasing to accompany the radiatively driven ground cooling. In the present study, the LT stability function proposed by Delage (1997) and later largely used in the literature (Bélair et al. 1999; Cuxart et al. 2006) has been used:

$$f_m(\mathrm{Ri}) = (1 + 12\mathrm{Ri})^{-1}. \tag{15}$$

The model has been, therefore, ran in four different configurations, combining the two different turbulent closures and the two different stability functions (Table 1).

TABLE 1. Different models that are compared in this work. With two closure orders and two stability functions, four different turbulence configurations are performed. For simplicity, the term "model" will be used hereafter to designate each configuration.

Model configuration	Closure	K_M	f_m(Ri)
1st short tail (1st ST)	First order	Eq. (7)	Eq. (14)
1st long tail (1st LT)	First order	Eq. (7)	Eq. (15)
E–l short tail (*E–l* ST)	*E–l*	Eq. (10)	Eq. (14)
E–l long tail (*E–l* LT)	*E–l*	Eq. (10)	Eq. (15)

c. Discretization and boundary conditions

The vertical discretization of Eqs. (1)–(3) and (11), for the *E–l* model, is done in a linearly varying mesh spacing proposed by Degrazia et al. (2009). To increase the resolution on the upper domain the grid increment was modified and written as (Schmengler et al. 2015)

$$\Delta z = \left[\left(\frac{1}{A}\right) + B\right] z_{l_i}, \tag{16}$$

where z_{l_i} is the height above the surface for a linear equally spaced grid, and A and B are arbitrary constants that should be modified to fit the domain size and number of levels. For a 6000-m-high domain, split in 252 levels from the surface to the domain top, the constants in Eq. (16) are $A = 1033.2$ and $B = 143.5$.

The first mass level, just above the surface, is located at $z_1 = 0.189$ m and the last level, just below the domain top, is located at $z_{251} = 5952.38$ m, so that Δz is smaller than 50 m in the upper part of the domain. The flux levels (zi_i) are located in between subsequent mass levels (z_i): $\mathrm{zi}_i = (z_{i+2} + z_i)/2$. The eddy diffusivities and the turbulent fluxes are evaluated at the flux levels. The prognostic equation for mean quantities [Eqs. (1)–(3)] are evaluated at the mass levels (z_i). In the *E–l* scheme, the prognostic equation for TKE [Eq. (11)] is evaluated at the flux levels (zi_i). The choice of a variable mesh grid is based in the well known fact that a low resolution near the surface can make the results dependent on the finite-difference method applied (Taylor and Delage 1971; Steeneveld et al. 2006).

The boundary conditions are defined as follows. At the domain top, the wind components and the potential temperature are set constant: $\overline{u}(t, z_{\mathrm{top}}) = \overline{u}_G$, $\overline{v}(t, z_{\mathrm{top}}) = \overline{v}_G$ and $\overline{\theta}(t, z_{\mathrm{top}}) = \Theta$. At the surface, the no-slip condition is assumed and the surface temperature decreases along the simulation with a constant cooling rate. The initial vertical profiles are: $\overline{u}(t = 0, z) = u_G$, $\overline{v}(t = 0, z) = \overline{v}_G$, and $\overline{\theta}(t = 0, z) = 265$ K up to 100 m, increasing at a constant lapse rate of 0.01 K m^{-1}, from that height until the domain top. For the *E–l* models, a minimum TKE

of $\overline{e}_{\min} = 10^{-9}\,\mathrm{m^2\,s^{-2}}$ is assumed to provide numerical stability (Mellor and Yamada 1982; Cuxart et al. 2006). Initial TKE is set equal to $0.4(1 - z/250)^3\,\mathrm{m^2\,s^{-2}}$ from the surface to 250 m, and it is assumed as $\overline{e}_{\min}$ above that height until the domain top (Cuxart et al. 2006). For very weak wind simulations, the residual TKE above the boundary layer height h is set as $\overline{e}_{\min}$ at all times, to avoid the influence of residual turbulence on the model solutions.

The set of prognostic equations Eq. (1), (2), (3), and (11) in the *E–l* model have been integrated for 10 h, using a fourth-order Runge–Kutta scheme (ReVelle 1993; McNider et al. 1995; Van de Wiel et al. 2002a; Costa et al. 2011, among others). A time step of 0.1 s has been used in all simulations. It has been chosen after a numerical sensitivity test of the results to the time step was performed.

The influence of the thermal forcings at the surface are represented by five constant cooling rates: 0.10, 0.25, 0.50, 1.00, and $2.50\,\mathrm{K\,h^{-1}}$. Here, the cooling rates are assumed as an external parameter, but it must be noted that in the real world it is not so. Surface cooling rates are in reality an internal parameter that depends, itself, on a number of other external properties, such as the radiative balance and soil physical properties and other internal ones, such as the surface heat flux. In the present case, the role of the external factors have been combined in a single external parameter, regarded as the cooling rate. The similar approach has been used in previous modeling studies (Kosović and Curry 2000; Weng and Taylor 2003, 2006; Cuxart et al. 2006; Acevedo et al. 2012, among others). The simulations have been performed for a wide range of range of geostrophic wind speeds $[U_G = (\overline{u}_G^2 + \overline{v}_G^2)]$, varying from 0.2 up to $30\,\mathrm{m\,s^{-1}}$, with increments of $0.2\,\mathrm{m\,s^{-1}}$. In reality, it is highly unlikely that geostrophic wind speeds and cooling rates are both very large or are both very small at the same time, so the simulation of these combined extreme cases must be regarded as a modeling exercise only. To describe the SBL regimes, the analysis will focus in a 100-m layer.

Every simulation starts after the evening transition. Therefore, the only way for the model to produce a neutral boundary layer ($\overline{w'\theta'} = 0$) is if no surface cooling rate exists. The analysis presented here refer to a quasi-equilibrium state, after 9 h of simulation.

d. Model validation

A model validation has been performed using GEWEX Atmospheric Boundary Layer Study (GABLS) I case (Kosović and Curry 2000) as a control. Figure 1 shows the comparison of all four configurations of the SCM (given in Table 1) with GABLS I experiment. The mechanical forcing and the thermal forcing used in the validation are $U_G = 8.0\,\mathrm{m\,s^{-1}}$ and a $0.25\,\mathrm{K\,h^{-1}}$ cooling rate.

The model boundary layer height is defined as the height where the sensible heat flux decreases to 5% of its surface value. Figure 1a shows that h is overestimated by all configurations of the model. However, when an ST stability function is used both 1st ST and *E–l* ST solutions are close to the GABLS I case. On the other hand, the use of an LT stability function leads to a thicker SBL. The 1st LT SBL is almost 140 m deeper than the *E–l* LT. Although all schemes reproduce the u_* temporal tendencies near the surface, they also underestimate its value (Fig. 1b).

All models reproduce the formation of the nocturnal jet (Fig. 1c). However, the 1st LT model overestimates the jet height by about 150 m, while the *E–l* model with long-tail stability function overestimates it by 30 m. It occurs because, as showed in Fig. 1a, these models reproduce a thicker SBL. It is caused mainly because an LT stability function allows the existence of turbulence at levels where an ST stability function does not. As a consequence, the SBL becomes more turbulent and homogeneous. Being more turbulent, in LT models the warm air from the top gets more easily transported toward the SBL bottom, increasing the air temperature near the surface as well (Fig. 1d). On the other hand, ST models are colder near the surface, even though they are more turbulent at these levels (Fig. 1b). The vertical structure of turbulence in the boundary layer is shown by the TKE profiles in Fig. 1e. As shown in Fig. 1b, the *E–l* LT scheme is less turbulent near the surface. However, turbulence in this scheme reaches higher levels than it does in the ST schemes. As previously mentioned, it happens because, allowing turbulence in the very stable regime, LT stability functions produce a deeper SBL.

The eddy diffusivity analysis (Figs. 1f,g) shows that the SBL turbulent diffusion is best represented by the *E–l* ST model, while 1st order schemes provide too much diffusion near the surface and, as a consequence, the turbulent fluxes also becomes larger in these cases (Figs. 1h,e,i). Figure 1h shows that the turbulent momentum fluxes are larger near the surface in the 1st models while the *E–l* model represents better the vertical distribution of this flux. Although all schemes are able to reproduce fairly well the eddy diffusivities and the momentum flux $[\tau/\rho = (\overline{u'w'}^2 + \overline{v'w'}^2)^{1/2}]$, they underestimate the sensible heat flux near the surface (Fig. 1i).

In general, the performance (Fig. 1) of all schemes is in agreement with previous studies that used GABLS I case as control (Cuxart et al. 2006; Weng and Taylor 2006).

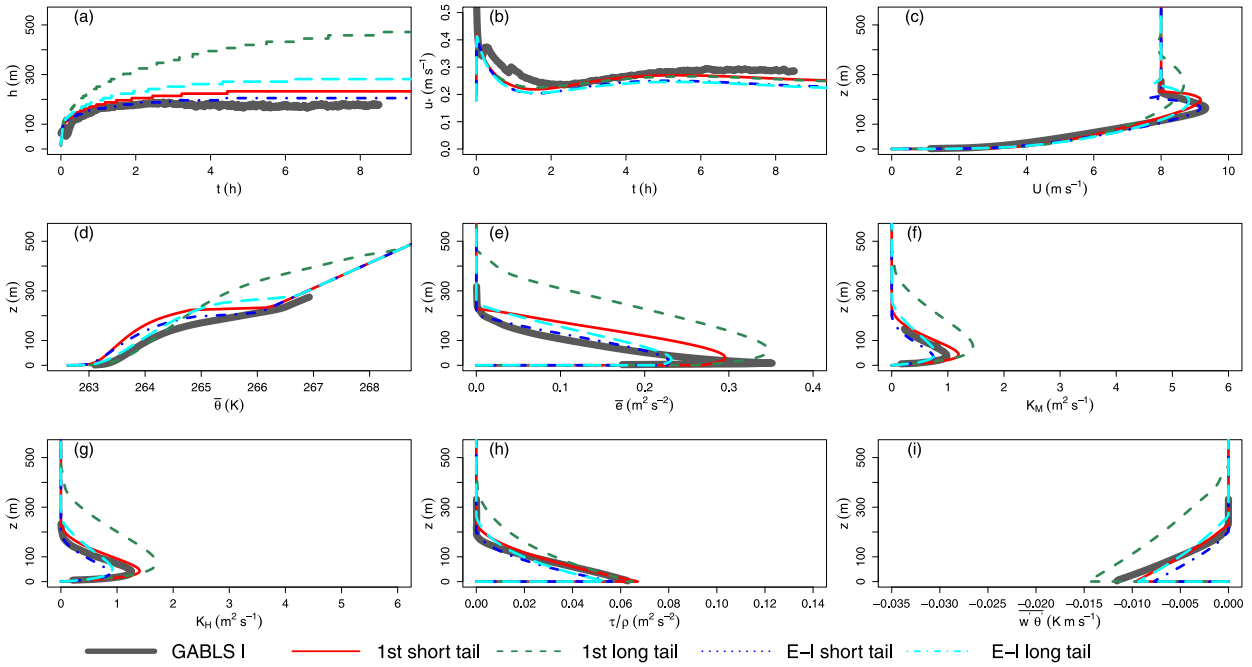

FIG. 1. (a) SBL height and (b) friction velocity time series. Vertical profiles of (c) wind speed, (d) temperature, (e) TKE, (f) momentum eddy diffusivity K_M, (g) heat eddy diffusivity K_H, (h) momentum flux, and (i) sensible heat flux. The solid thick gray line is the GABLS I case; red dashed line is the 1st ST model; green dashed line is the 1st LT model; blue dashed line is the *E–l* ST model; and the cyan dashed line is the *E–l* LT model.

3. Results

Observational studies of the SBL regimes, such as those from Sun et al. (2012), Acevedo et al. (2016), and Lan et al. (2018), used tower observations to determine a mean wind speed threshold below which the VSBL exists and above which the WSBL exists. Such thresholds are determined by wind speed observation either at the same level of the turbulence observations (Sun et al. 2012) or near the ground (Acevedo et al. 2016). In both cases, the wind observations are affected by turbulent mixing activity, making the thresholds dependent on the internal SBL dynamics. van der Linden et al. (2017) attempted to overcome this difficulty by classifying the SBL structure in terms of geostrophic wind speed, using the long-term measurements at the Cabauw tower for that purpose. However, they could not associate a geostrophic wind threshold to an abrupt change of the SBL structure, possibly because the averaging over a large number of cases smoothed characteristics that are abrupt for individual occurrences alone. In the single-column models, on the other hand, the SBL environment is controlled and the geostrophic forcing is precisely determined in each case. For this reason, in the present study the regime classification is done in terms of the external forcing, given by the geostrophic wind. Besides, there is no need to refer to the quantities near the ground only, as is typically done in observational studies. Rather, in the present case, the main vertical level chosen for the analysis is 100 m, which in many cases is both far from the ground and from the SBL top. Besides, it is a level high enough to analyze the transitions experienced as turbulence first reaches it and later becomes strong. Figure 1c showed that in the validation experiment, regardless of the scheme, the mean wind speed increases sharply with height near the ground, reaching a maximum U_{MAX} some meters below the SBL top. Above the SBL, where TKE is zero (Fig. 1e), the mean wind speed is geostrophic. Since this structure is valid for all schemes considered, it is always possible to determine three different regimes in any given vertical profile in the model:

- At the uppermost layer, where $U = U_G$, the flow is laminar.
- Just below the laminar layer and above the height of U_{MAX} there is a very stable layer (VSL), which has weak turbulence and presents a large thermal gradient (Fig. 1d). Such a VSL presents peculiar characteristics that will be discussed along the present study.
- Below the height where U_{MAX} occurs, turbulence is much stronger than in the VSL and a weakly stable layer (WSL) exists, as supported by the reduced thermal gradient (Fig. 1d).

This classification strategy implies that in any circumstance there is a WSL and a VSL at the same time, but at different layers. At first sight, it contrasts with the strategy commonly used in observational studies that define a given regime for the entire SBL at any given time (Mahrt et al. 1998; Sun et al. 2012; van Hooijdonk et al. 2015; Acevedo et al. 2016; Lan et al. 2018, among many others). In reality, however, there is consistency between the two classification strategies, because the WSL may be present below any given observational level after the transition. This is, in fact, supported by observations that show that very close to the ground the SBL is nearly always at the strong wind, weakly stable regime (Sun et al. 2012, 2015).

Figure 2 shows the wind (left panels) and TKE (center panels) profiles at the relevant transitions for the 100-m level: when turbulence arrives at that level (black lines), when it reaches U_{MAX}, which is the VSL to WSL transition (red lines). In all cases a $0.25\,K\,h^{-1}$ cooling rate was assumed.

The temperature difference between 100 m and the surface ($\Delta\theta$; Fig. 2, right panels) is independent on the geostrophic wind until turbulence reaches 100 m, marking the onset of the VSL. As U_G increases further, this temperature difference decreases sharply, with the largest $\Delta\theta$ dependence on U_G occurring at the VSL–WSL transition. When the 100-m level is within the WSL, its temperature difference from the surface decreases slightly with U_G and for large U_G, the temperature gradient becomes almost independent on U_G (notice the logarithmic horizontal axis in the right panels of Fig. 2). For very large U_G, $\Delta\theta$ increases with U_G because in this case turbulence has reached higher levels, bringing downward the warm air from above 100 m. van der Linden et al. (2017) have observed a similar slight increase of $\Delta\theta$ with U_G for $U_G > 15\,m\,s^{-1}$ in the Cabauw tower. This general S-shape dependence of the temperature gradient on wind speed has been found in both experimental (Acevedo et al. 2016; van der Linden et al. 2017; Mahrt 2017; Vignon et al. 2017) and modeling studies (Van de Wiel et al. 2017; Baas et al. 2018). Besides, the VSL–WSL transition coincidence with the largest thermal gradient dependence on U_G has also been suggested by Van de Wiel et al. (2017), as the SBL regime transition. Figure 2 also shows that all model schemes reproduce the SBL regime transitions, despite their peculiarities. The differences between the schemes and how they reproduce the turbulent and thermal vertical structures will be discussed in detail next, along with an analysis on how they depend on the SBL regime.

In agreement with previous studies based on simplified models (Acevedo et al. 2012; Van de Wiel et al. 2017; Maroneze et al. 2019b), the transition characteristics depend on the scheme used. The differences on their representation of the VSL–WSL transition become clear when the relationship between V_{TKE} and the local wind is analyzed (Fig. 3). The laminar–turbulent (L–T) transition occurs when V_{TKE} exceeds its minimum value and starts increasing with the wind speed. This is a small increase, more evident in the short-tail schemes (Figs. 3a,c) and at higher levels. The VSBL–WSBL transition, indicated by the triangles in the bottom of the panels, occurs when the V_{TKE} dependence on U changes, in agreement with the observations from Sun et al. (2012). In the short-tail schemes this change is such that V_{TKE} abruptly increases with a small increase of U. In the long-tail schemes, on the other hand V_{TKE} steadily increases with U once such a transition, which is not abrupt, takes place. The wind threshold for the VSL–WSL transition depends on the formulation. Long tail schemes generally provide more turbulence for the same U_G. In the 1st LT scheme, all levels up to 10 m are coupled, even for very light winds (Figs. 3b). The transition occurs at a low wind threshold in the *E–l* long tail scheme. On the other hand, the least turbulent scheme, *E–l* ST, has the largest U thresholds for the VSL–WSL transition.

If the surface cooling rate increases, the thermal gradient also increases, and larger wind shear becomes necessary to generate and maintain turbulence in the flow. Figure 4 shows the relationship between V_{TKE} and U at 10 m for different cooling rates. In the ST schemes, the wind threshold for the VSL–WSL transition increases almost $4\,m\,s^{-1}$ for cooling rates varying from 0.1 to $2.5\,K\,h^{-1}$. In contrast, for the 1st LT scheme, the wind threshold for the transition shows almost no dependence on the surface cooling rate, because the LT function provides more mixing the transition occurs with a smaller value of U. Consecutively, with small cooling rates the levels near the surface are in the WSL. In this case, for cooling rates larger than $0.5\,K\,h^{-1}$, the model solves a VSL at 10 m (Fig. 4b), but the laminar layer occurs at that height. Being long tail, the *E–l* LT is also turbulent at large Ri, but in this case a laminar boundary layer occurs near the surface for large cooling rates (Fig. 4d), contrasting with the 1st LT in that respect. Such a reduced sensitivity of LT schemes to the cooling rate has been previously found by McNider et al. (2012). Figure 4 also shows that near the surface the relationship between V_{TKE} and U becomes nearly independent on both the turbulence scheme and the cooling rate for large values of U. Furthermore, Fig. 4 shows that, in the ST schemes and for large cooling rates, there is a region where V_{TKE} decreases as U increases. This is caused by a maximum in the wind speed profile that does not exist in V_{TKE}. In a practical sense, V_{TKE} may assume two

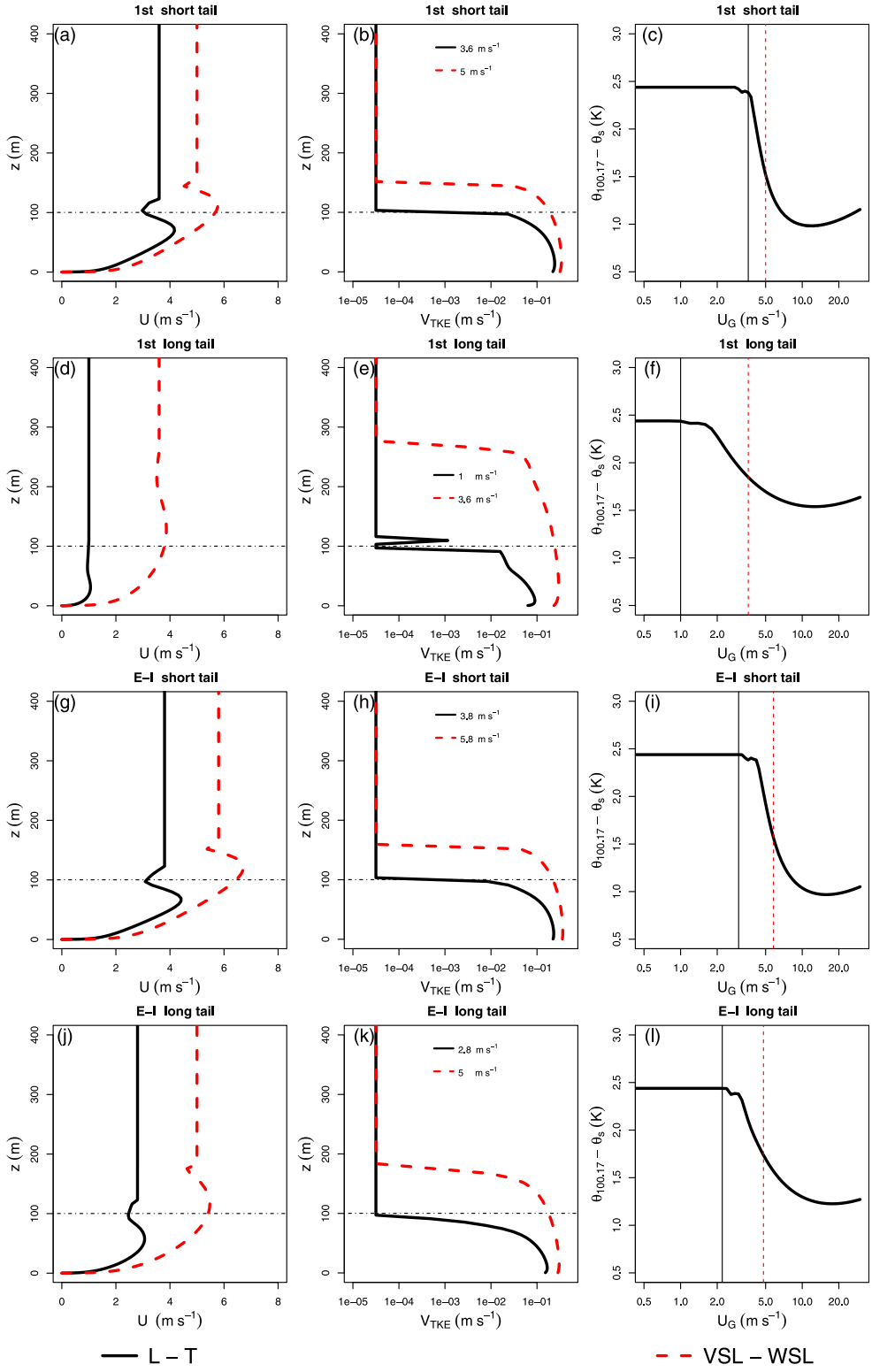

FIG. 2. The ninth-hour mean vertical profiles of (left) U and (center) V_{TKE}; (right) thermal gradient in a 100-m layer. The transition is analyzed in a 100-m layer (black horizontal dashed lines in the profiles panels). The mechanical forcing for each profile is indicated in the legend of the center panels. In the left and center columns, the black solid line is the vertical profile when turbulence reaches the 100-m level, and the red

different values for the same local wind speed. However, it does not characterize a bistable regime, as U is a local variable, rather than an external parameter. It does not occur when V_{TKE} is analyzed in terms of U_G, showing that V_{TKE} increases monotonically with the external mechanical forcing.

At 100 m, laminar flow occurs with light winds and large cooling rates in all schemes, so that both L–T and VSL–WSL transition are evident in all cases. When the flow is laminar at that level, the entire SBL exists below it, being therefore shallower than 100 m (Fig. 5). As U_G and, therefore, the 100-m wind increase, turbulence reaches higher levels, so that eventually the SBL reaches the 100-m level and beyond. These results explain why the outputs of numerical weather prediction models near the surface are highly dependent on the boundary layer scheme in light wind conditions but not as much in the strong wind case (Battisti et al. 2017).

Stability parameters that relate the thermal and mechanical properties of the flow are often used to classify the SBL regimes (Nieuwstadt 1984; Mahrt et al. 1998; Van de Wiel et al. 2002b; van Hooijdonk et al. 2015; Lan et al. 2018, among others). One of such parameters, the local gradient Richardson number, affects the solutions, as in the ST schemes [Eq. (14)] turbulence only exists when $\mathrm{Ri} < \mathrm{Ri}_c$, so that the L–T transition occurs for $\mathrm{Ri} = \mathrm{Ri}_c = 0.2$ (figure not shown). In LT schemes, on the other hand, there is turbulent mixing for any Ri. Nevertheless, it has been shown in the previous figures that the VSL–WSL transition also occurs in that case. Does VSL–WSL transition happen at a given value of Ri? Do other stability parameter have a critical value for the transition? As the schemes have different dependencies on Ri, it is not appropriate to define the VSL–WSL transition in terms of Ri. Mahrt (2010) suggested that the bulk Richardson number (Rb) is a measure of the whole stability of the layer that is less vulnerable to errors and self-correlations with high-order turbulence moments, such as the heat flux:

$$\mathrm{Rb} = \frac{g}{\Theta}\frac{\theta(z) - \theta_s z}{U(z)^2}. \tag{17}$$

In Eq. (17), $\theta(z)$ and $U(z)$ are temperature and mean wind speed at a height z above the ground and θ_s is the surface temperature. While Ri describes the local stability of the flow, Rb is a measure of the overall stability of an arbitrary layer. Thus, there is no a priori critical value for Rb, and its value at the transition may vary. Recently, van Hooijdonk et al. (2015) showed that commonly used scaling parameters, such as Ri and z/L, do not have a critical value that splits between the very stable and weakly stable regimes. They proposed a new dimensionless parameter, the shear capacity of the flow (SC), which should be able to predict the transition. The shear capacity definition considers that the regime transition coincides with the heat flux maximum and that there is a minimum wind speed below which turbulence cannot be continually sustained (Van de Wiel et al. 2012b). SC is defined in terms of bulk properties as (van Hooijdonk et al. 2015)

$$\mathrm{SC} = U\left\{\frac{g}{\Theta\kappa^2} Hz[\ln(z/z_0)]^2\right\}^{-1/3}, \tag{18}$$

where H is the absolute value of the surface heat flux, z is the height over the surface, and $z_0 = 0.1$ m is the roughness length.

The meaning of the dimensionless numbers values in terms of the model regimes can be understood when the sensible heat flux convergence between the surface and 100 m ($H_{1.51\mathrm{m}} - H_{97.13\mathrm{m}}$) is determined as a function of the external parameters U_G and cooling rate (Fig. 6). All schemes show a similar qualitative dependence, expressed by the gray contour lines. For weak winds the average flux convergence is independent on the cooling rate, increasing only as U_G increases. It happens because turbulence has not reached 100 m yet. The laminar–turbulent transition at 100 m takes place when the contour lines at Fig. 6 start to bend. At this point, the flux convergence becomes also dependent on the cooling rate. In the other extreme, for large wind speeds, the heat flux convergence is only dependent on the cooling rate (Fig. 6). The values for U_G at the VSL–WSL transition shown in Fig. 2 are presented as black crosses in Fig. 6. They happen when the flux convergence contour lines have maximum curvature, meaning that the transition happens when the flux convergence is most dependent on both cooling rate and U_G. The bulk stability parameters generally have a critical value that defines the transition. However, such a critical value varies among the schemes. In both ST models Rb = 0.2 is very close to the VSL–WSL transition, while the same occurs for SC = 3.1 and 3.3, but in this case for small cooling rates only. For the 1st LT scheme, the critical values are

←

dashed line is vertical profile on the VSL–WSL transition. Vertical lines in the right column correspond to the values of U_G presented by the respective colors in each center panel. Each model is indicated in the panel title and the surface cooling rate used in all cases was 0.25 K h^{-1}.

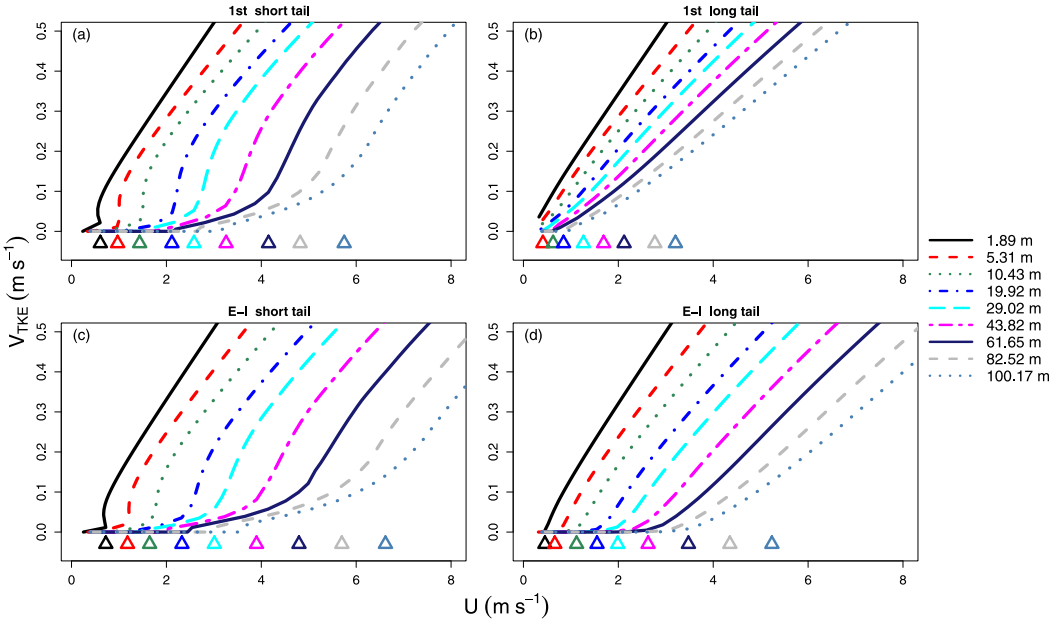

FIG. 3. Average dependence of V_{TKE} and the local wind speed U for the levels indicated in the legend. The triangles along the bottom of each panel indicate the value of U at which the VSL–WSL transition, defined in Fig. 2, occurs. All simulations use a constant cooling rate of 0.25 K h^{-1}. The relationship represents the mean of the ninth hour of each simulation.

Rb = 1.0 and SC = 2.0, while in the *E–l* LT case the transition happens at Rb = 0.5 and SC = 3.1. The transition value of SC in the ST models, between 3 and 3.5 is similar to those found by van Hooijdonk et al. (2015) using Cabauw observed data. On the other hand, the transition Rb, near 0.2, is larger than those found by Mahrt (2017) using Fluxes over a Snow Surface (FLOSS) II data and than the theoretical value

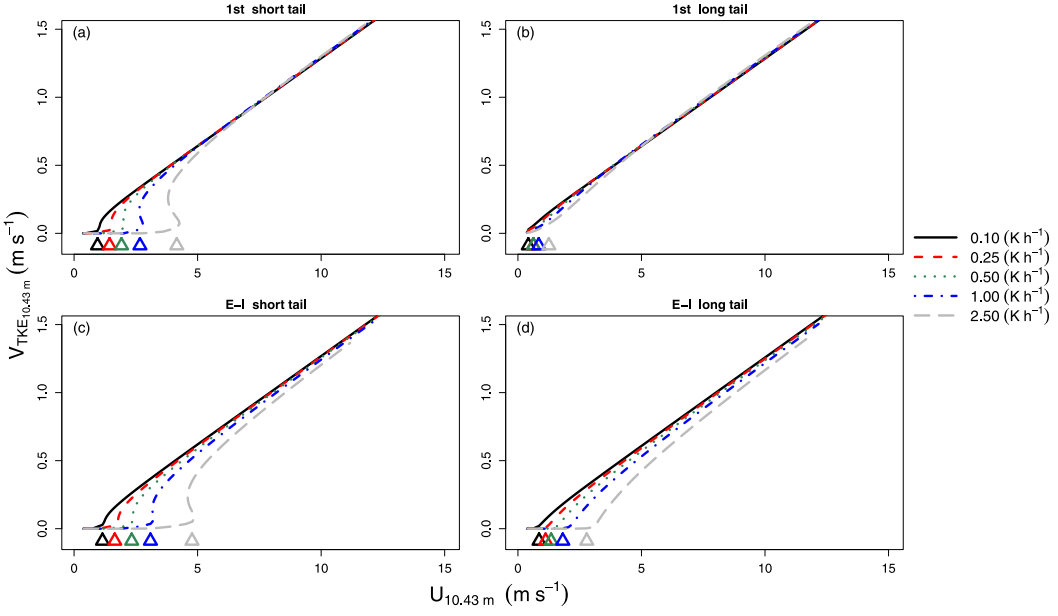

FIG. 4. Relationship between V_{TKE} and U at 10.43 m above the surface. The surface cooling rates are 0.1 (solid black line), 0.25 (red dashed line), 0.5 (green dashed line), 1.0 (blue dashed line), and 2.5 K h^{-1} (gray dashed line). The relationship represents the mean of the ninth hour of each simulation. The triangles along the bottom of each panel indicate the value of U at which the VSL–WSL transition, defined in Fig. 2, occurs.

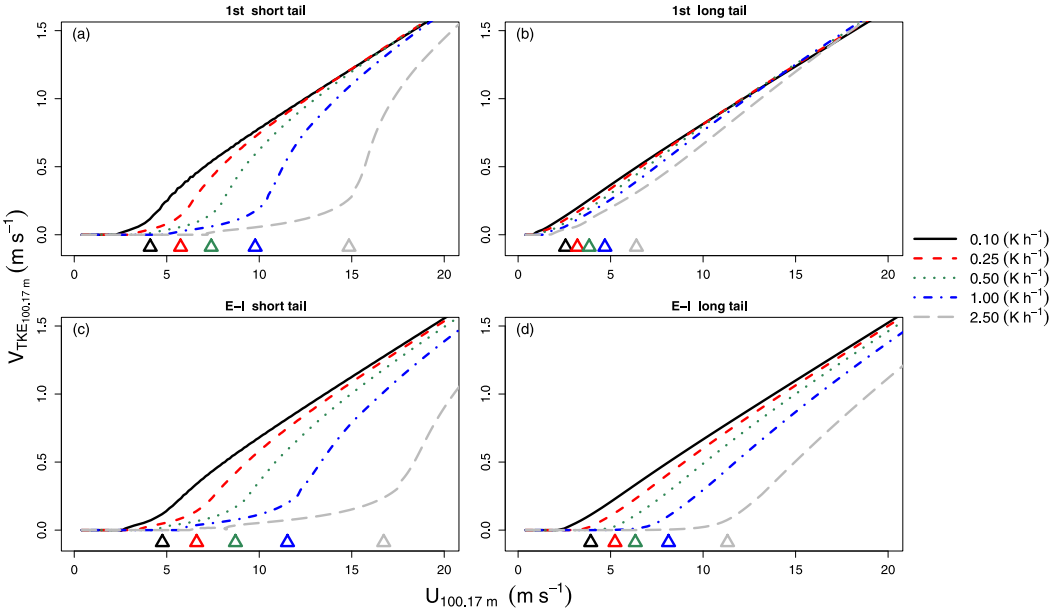

FIG. 5. As in Fig. 4, but for the 100-m level.

proposed by Van de Wiel et al. (2017), but this difference is probably a consequence of the estimations being made over different depths. These critical values must be considered as approximations, as their coincidence with the transition is variable, specially for large cooling rates. van Hooijdonk et al. (2015) suggested that it is possible to either use internal flow parameters or boundary conditions to scale the flow in the SBL. Along this line, Rb can only be used if it is defined in terms of parameters at the level considered and/or below it, as the layers above it may be in an entirely different regime. In other words, an internal Rb must be chosen. On the other hand, the same does not apply to SC, which, being dependent on the surface heat flux (boundary condition) and the wind speed at a fixed level, is less dependent on the levels chosen for its evaluation. It is,

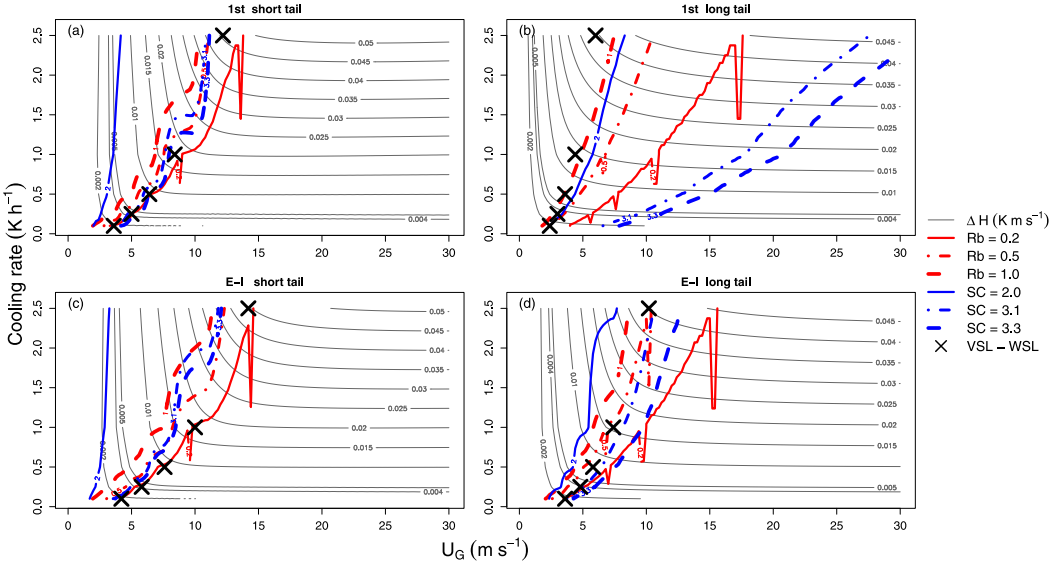

FIG. 6. Average dependence of the absolute heat flux difference over 100 m ($H_{1.51m} - H_{100m}$) on the surface cooling rate and the geostrophic wind (solid gray contours). Red lines are Rb = 0.2 (solid), Rb = 0.5 (dot–dashed), and Rb = 1 (dashed). Blue lines are SC = 2.0 (solid), SC = 3.1 (dot-dashed), and SC = 3.3 (dashed). The stability parameters were evaluated considering the z = 100-m layer. Black crosses indicate the value of U_G at which the VSL–WSL transition, defined in Fig. 2, occurs over 100 m.

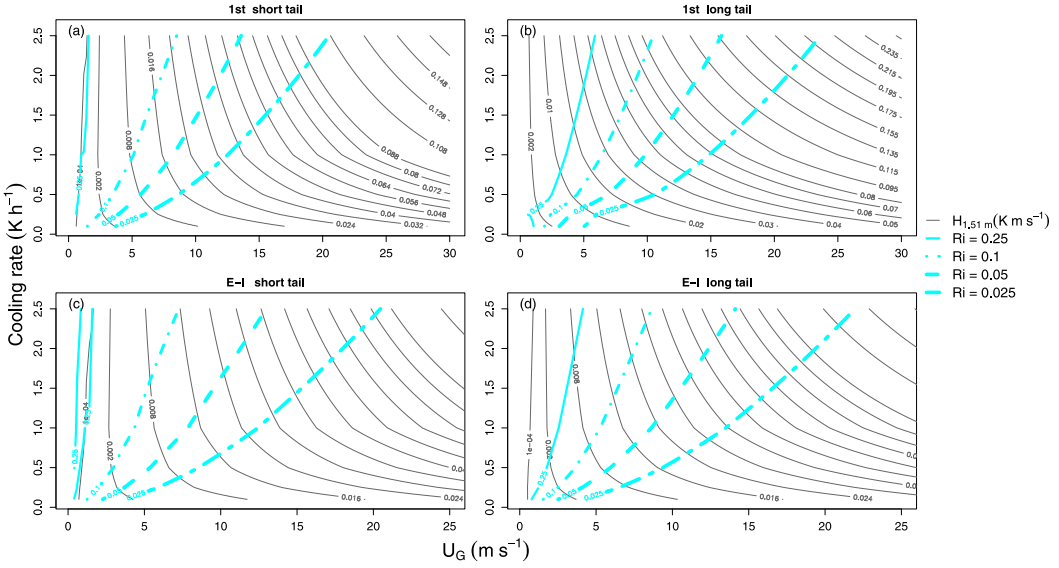

FIG. 7. Joint average distribution of the surface heat flux on the surface cooling rate and on the geostrophic wind (solid gray contours). Light blue lines are the local gradient Richardson gradient: Ri = 0.2 (solid), Ri = 0.1 (dot–dashed), Ri = 0.05 (dashed), and Ri = 0.025 (short–long dashed).

therefore, a more universal parameter, which may be used to describe the stability of a layer deeper than that used on its evaluation.

All schemes show similar heat flux dependence on the external parameters U_G and cooling rate (Fig. 7). For very light winds H is independent of the surface cooling rate and solely dependent on U_G for the ST schemes, while it is slightly dependent on the cooling rate for the LT cases. Therefore, for weak winds, only the wind intensity controls the heat flux (VSL). Once the VSL–WSL transition takes place, both external parameters play important roles on H behavior. Similar relationships have been observed at the FLOSS II and Shallow Cold Pool (SCP) experiments by Mahrt (2017), who showed the joint distribution of the heat flux in terms of the vertical temperature difference $\delta\theta$ and the local wind. For the ST schemes, the heat flux is independent on the cooling rate when Ri $>$ 0.25, as the flow in such

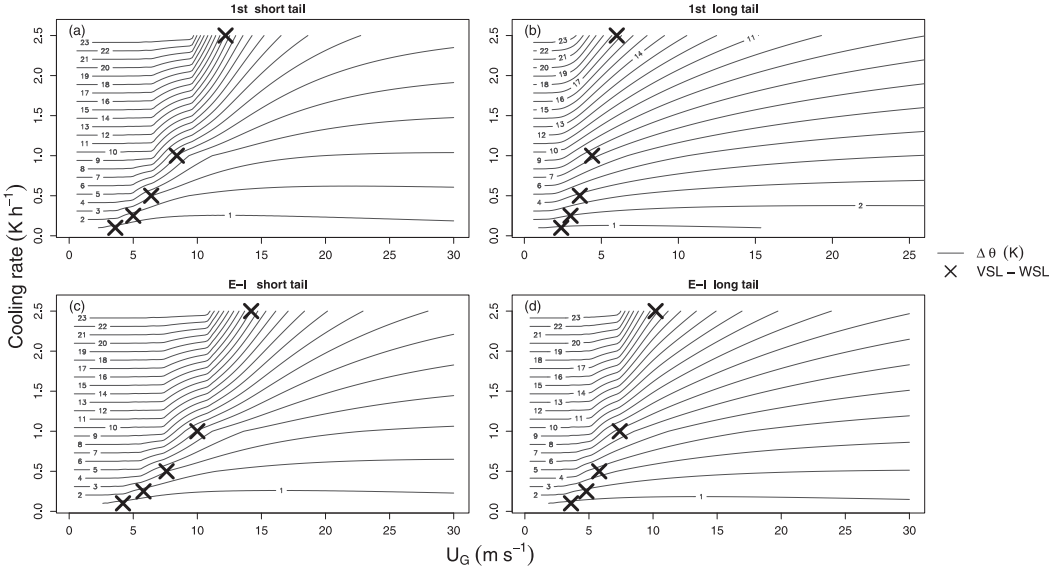

FIG. 8. Average dependence of the temperature gradient between 100 m and the surface ($\Delta\theta = \theta_{100\mathrm{m}} - \theta_s$) on the surface cooling rate and the geostrophic wind (solid gray contours). Black crosses indicate the value of U_G at which the VSL–WSL transition, defined in Fig. 2, occurs over 100 m.

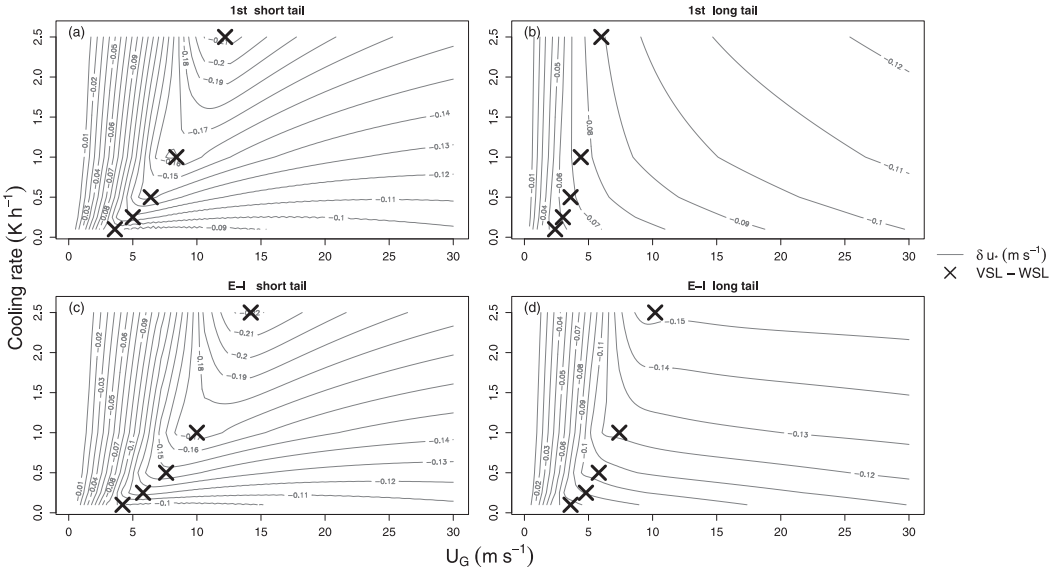

FIG. 9. As in Fig. 8, but for δu_*.

case is laminar. In the more turbulent LT schemes, on the other hand, the heat flux always depends on the cooling rate, although for light winds this dependence is small (Figs. 7b,d). The Ri contours are very similar to those presented by Mahrt (2017), despite the fact that here the comparison is done to the cooling rate where Mahrt (2017) used the local thermal gradient.

The potential temperature difference between 100 m and the surface ($\Delta\theta$) is independent on U_G and solely dependent on the cooling rate for both the small and large limits of U_G (Fig. 8). For very weak U_G, the SBL is shallower than 100 m, therefore being unaffected by changes in the geostrophic forcing. When turbulence first reaches 100 m (L–T transition), the contour lines in Fig. 8 depart from the horizontal. In this case, cold air from lower levels is brought up, decreasing $\Delta\theta$. The maximum dependence of $\Delta\theta$ on the geostrophic wind coincides exactly with the VSL–WSL transition (crosses in Fig. 8). From this point on, increases in U_G increasingly mix the air from the surface to 100 m, causing $\Delta\theta$ to decrease at a slower rate with increasing U_G. This is an important result because it indicates that the transition happens when the vertical thermal gradient dependence on the wind speed is largest. These are two simple variables, frequently observed in standard weather stations, so that this result may provide a means for finding the wind speed threshold for the transition from such simple observations.

Mahrt et al. (2018) analyzed the vertical difference of the friction velocity u_* between two levels (δu_*) in terms of the vertical temperature gradient and the mean wind speed, using data collected at the FLOSS II and SCP experiments. They found that the "traditional boundary layer" behavior of δu_* decreasing with increasing wind speed (for a fixed thermal gradient) and decreasing with increasing thermal gradient (for a fixed mean wind speed) is only found for large enough wind speeds because for very weak winds there is horizontal advection of u_* aloft, causing negative values of δu_*. Here, the joint distribution of δu_* in terms of the cooling rate and geostrophic wind speed is analyzed, as these are the two main external factor affecting the simulations. The "traditional boundary layer" behavior reported by Mahrt et al. (2018) is evident regardless of the wind speed, as no horizontal advection of any kind exists in the model, but only for the short-tail schemes (Figs. 9a,c). In these cases, the minimum δu_* for a given cooling rate occurs exactly at the VSL–WSL transition. For the long tail schemes, the VSL–WSL transition coincides with maximum curvature of the joint distribution of δu_* shown in Fig. 9.

4. Discussion and conclusions

The numerically simulated stable boundary layer (SBL) experiences regime transitions, regardless of the turbulence parameterization order and stability function used. The flow presents a three-layer structure: next to the surface there is a layer where turbulence is strong enough to reduce the thermal gradient, a layer above that where turbulence is reduced and does not affect the thermal gradient largely, and a laminar layer above the other two and toward the domain top. The lowest layer is consistent with the common classification of a weakly stable layer with reduced thermal gradients and

the intermediate one is in the very stable state, with larger thermal gradients. The laminar regime at the uppermost layer corresponds to the decoupled state defined by Derbyshire (1999) and present in the solutions of previously presented simplified models (McNider et al. 1995; Van de Wiel et al. 2002a; Costa et al. 2011; Acevedo et al. 2012). Both in the weakly stable and in the laminar regimes, the temperature gradient is nearly independent of the geostrophic wind, being solely dependent on the prescribed surface cooling rate. The intermediate very stable regime is, therefore, characterized as the only condition when the thermal gradient changes with the large-scale mechanical forcing. Under very weak geostrophic winds, it is possible that only the very stable and the laminar layer exist, or even that the flow is entirely laminar. This result is directly related to the fact that the numerical weather prediction models results, near the surface, are highly dependent on the boundary layer scheme, while the same does not occur under strong wind conditions.

In this three-layer framework, a given vertical level experiences a SBL regime transition when the boundary between two adjacent layers crosses that level. When it occurs for the boundary between the uppermost laminar layer and the intermediate very stable layer, it marks the laminar–turbulent (L–T) transition. The level experiencing such transition at any time may be regarded as the top of the SBL. When the boundary from the very stable layer and the lowest weakly stable layer crosses a level, it experiences the very stable to weakly stable (VSL–WSL) transition. Given that the entire analysis is based on the equilibrium states of the simulation, the opposite transitions (T–L and VSL–WSL) happen at the same conditions when the geostrophic wind decreases instead of increasing.

It has been shown that the S-shaped dependence of the thermal gradient on the mean wind speed, observed by Acevedo et al. (2016), Vignon et al. (2017), Mahrt (2017), and Baas et al. (2018) is well reproduced by the single-column models (Fig. 2, right column). Furthermore, the model analysis allows associating the proposed three-layer structure, solely derived from the model outputs, with specific relationships between the thermal gradient and the mean wind speed. In the laminar layer, located above the SBL, the thermal gradient is independent on the mean wind speed. In the very stable layer, below the SBL top, the thermal gradient varies largely with the local wind speed. Underneath, the weakly stable layer, that may be very shallow, is characterized by a thermal gradient that varies little with the local wind speed. The model behavior of the vertical gradient of friction velocity δu_* between two levels may also be compared to a similar observational analysis, performed by Mahrt et al. (2018). They have shown that such a gradient is nearly independent of the mean wind speed for intense winds, while for weak winds, δu_* is nearly independent on the thermal gradient. In the single-column models, an equivalent independence on the cooling rate occurs (Fig. 9). Both in the observations and the model, the latter behavior occurs because the near-surface generated turbulence has not yet reached the upper level of analysis. These examples show that many aspects of the model behavior are determined by the same causes observed in nature. However, the confirmation that the three-layer structure observed in the model also occurs in nature still demands a detailed observational study.

In the real world, the radiative balance and the physical soil properties have a key role in controlling the SBL regime (Van de Wiel et al. 2017; Maroneze et al. 2019a). In this study, these processes have been combined in the prescribed cooling rate, that is, for this reason, regarded as an external parameter, while in reality it also depends on some internal SBL processes, such as the turbulent heat flux. This approach has been previously adopted in other modeling studies (Kosović and Curry 2000; Weng and Taylor 2003, 2006; Cuxart et al. 2006; Acevedo et al. 2012, among others) but, nevertheless, a detailed modeling comparison that explicitly incorporates these processes and others, such as horizontal advection and radiative flux divergence in the atmosphere, is still necessary.

Acknowledgments. This paper has been developed as part of the Research and Technological Development Project of Brazilian electrical energy sector, regulated by National Electric Energy Agency (ANEEL), having received financial support from ENEVA S.A. The study was also supported in part by Conselho Nacional de Desenvolvimento Científico e Tecnológico (CNPq) (Grants FDC—426409/2016-7 and 313022/2018-6; OCA). This study was also financed in part by the Coordenação de Aperfeiçoamento de Pessoal de Nível Superior–Brasil (CAPES)—Finance Code 001. Three anonymous reviewers offered valuable comments and suggestions.

REFERENCES

Acevedo, O. C., F. D. Costa, and G. A. Degrazia, 2012: The coupling state of an idealized stable boundary layer. *Bound.-Layer Meteor.*, **145**, 211–228, https://doi.org/10.1007/s10546-011-9676-3.

——, ——, P. E. Oliveira, F. S. Puhales, G. A. Degrazia, and D. R. Roberti, 2014: The influence of submeso processes on stable boundary layer similarity relationships. *J. Atmos. Sci.*, **71**, 207–225, https://doi.org/10.1175/JAS-D-13-0131.1.

——, L. Mahrt, F. S. Puhales, F. D. Costa, L. E. Medeiros, and G. A. Degrazia, 2016: Contrasting structures between the decoupled and coupled states of the stable boundary layer. *Quart. J. Roy. Meteor. Soc.*, **142**, 693–702, https://doi.org/10.1002/qj.2693.

André, J., G. De Moor, P. Lacarrere, and R. Du Vachat, 1978: Modeling the 24-hour evolution of the mean and turbulent

structures of the planetary boundary layer. *J. Atmos. Sci.*, **35**, 1861–1883, https://doi.org/10.1175/1520-0469(1978)035<1861:MTHEOT>2.0.CO;2.

Ansorge, C., and J. P. Mellado, 2014: Global intermittency and collapsing turbulence in the stratified planetary boundary layer. *Bound.-Layer Meteor.*, **153**, 89–116, https://doi.org/10.1007/s10546-014-9941-3.

Baas, P., B. van de Wiel, S. van der Linden, and F. Bosveld, 2018: From near-neutral to strongly stratified: Adequately modelling the clear-sky nocturnal boundary layer at Cabauw. *Bound.-Layer Meteor.*, **166**, 217–238, https://doi.org/10.1007/s10546-017-0304-8.

Battisti, A., O. C. Acevedo, F. D. Costa, F. S. Puhales, V. Anabor, and G. A. Degrazia, 2017: Evaluation of nocturnal temperature forecasts provided by the Weather Research and Forecast Model for different stability regimes and terrain characteristics. *Bound.-Layer Meteor.*, **162**, 523–546, https://doi.org/10.1007/s10546-016-0209-y.

Bélair, S., J. Mailhot, J. W. Strapp, and J. I. MacPherson, 1999: An examination of local versus nonlocal aspects of a TKE-based boundary layer scheme in clear convective conditions. *J. Appl. Meteor.*, **38**, 1499–1518, https://doi.org/10.1175/1520-0450(1999)038<1499:AEOLVN>2.0.CO;2.

Blackadar, A. K., 1962: The vertical distribution of wind and turbulent exchange in a neutral atmosphere. *J. Geophys. Res.*, **67**, 3095–3102, https://doi.org/10.1029/JZ067i008p03095.

Costa, F. D., O. C. Acevedo, J. C. Mombach, and G. A. Degrazia, 2011: A simplified model for intermittent turbulence in the nocturnal boundary layer. *J. Atmos. Sci.*, **68**, 1714–1729, https://doi.org/10.1175/2011JAS3655.1.

Cuxart, J., and Coauthors, 2006: Single-column model intercomparison for a stably stratified atmospheric boundary layer. *Bound.-Layer Meteor.*, **118**, 273–303, https://doi.org/10.1007/s10546-005-3780-1.

Degrazia, G. A., U. Rizza, F. S. Puhales, A. G. Goulart, J. Carvalho, G. S. Welter, and E. P. Marques Filho, 2009: A variable mesh spacing for large-eddy simulation models in the convective boundary layer. *Bound.-Layer Meteor.*, **131**, 277–292, https://doi.org/10.1007/s10546-009-9360-z.

Delage, Y., 1974: A numerical study of the nocturnal atmospheric boundary layer. *Quart. J. Roy. Meteor. Soc.*, **100**, 351–364, https://doi.org/10.1002/qj.49710042507.

——, 1997: Parameterising sub-grid scale vertical transport in atmospheric models under statically stable conditions. *Bound.-Layer Meteor.*, **82**, 23–48, https://doi.org/10.1023/A:1000132524077.

Derbyshire, S., 1999: Boundary-layer decoupling over cold surfaces as a physical boundary-instability. *Bound.-Layer Meteor.*, **90**, 297–325, https://doi.org/10.1023/A:1001710014316.

Duynkerke, P., 1988: Application of the E–ε turbulence closure model to the neutral and stable atmospheric boundary layer. *J. Atmos. Sci.*, **45**, 865–880, https://doi.org/10.1175/1520-0469(1988)045<0865:AOTTCM>2.0.CO;2.

England, D. E., and R. T. McNider, 1995: Stability functions based upon shear functions. *Bound.-Layer Meteor.*, **74**, 113–130, https://doi.org/10.1007/BF00715713.

He, P., and S. Basu, 2015: Direct numerical simulation of intermittent turbulence under stably stratified conditions. *Nonlinear Processes Geophys.*, **22**, 447–471, https://doi.org/10.5194/npg-22-447-2015.

Holdsworth, A. M., and A. H. Monahan, 2019: Turbulent collapse and recovery in the stable boundary layer using an idealized model of pressure-driven flow with a surface energy budget. *J. Atmos. Sci.*, **76**, 1307–1327, https://doi.org/10.1175/JAS-D-18-0312.1.

Holtslag, A., and B. Boville, 1993: Local versus nonlocal boundary-layer diffusion in a global climate model. *J. Climate*, **6**, 1825–1842, https://doi.org/10.1175/1520-0442(1993)006<1825:LVNBLD>2.0.CO;2.

Katul, G. G., A. Porporato, S. Shah, and E. Bou-Zeid, 2014: Two phenomenological constants explain similarity laws in stably stratified turbulence. *Phys. Rev.*, **89E**, 023007, https://doi.org/10.1103/PhysRevE.89.023007.

Kosović, B., and J. A. Curry, 2000: A large eddy simulation study of a quasi-steady, stably stratified atmospheric boundary layer. *J. Atmos. Sci.*, **57**, 1052–1068, https://doi.org/10.1175/1520-0469(2000)057<1052:ALESSO>2.0.CO;2.

Lan, C., H. Liu, D. Li, G. G. Katul, and D. Finn, 2018: Distinct turbulence structures in stably stratified boundary layers with weak and strong surface shear. *J. Geophys. Res. Atmos.*, **123**, 7839–7854, https://doi.org/10.1029/2018JD028628.

Li, D., G. G. Katul, and S. S. Zilitinkevich, 2015: Revisiting the turbulent Prandtl number in an idealized atmospheric surface layer. *J. Atmos. Sci.*, **72**, 2394–2410, https://doi.org/10.1175/JAS-D-14-0335.1.

Louis, J.-F., 1979: A parametric model of vertical eddy fluxes in the atmosphere. *Bound.-Layer Meteor.*, **17**, 187–202, https://doi.org/10.1007/BF00117978.

Mahrt, L., 2010: Variability and maintenance of turbulence in the very stable boundary layer. *Bound.-Layer Meteor.*, **135**, 1–18, https://doi.org/10.1007/s10546-009-9463-6.

——, 2017: Heat flux in the strong-wind nocturnal boundary layer. *Bound.-Layer Meteor.*, **163**, 161–177, https://doi.org/10.1007/s10546-016-0219-9.

——, J. Sun, W. Blumen, T. Delany, and S. Oncley, 1998: Nocturnal boundary-layer regimes. *Bound.-Layer Meteor.*, **88**, 255–278, https://doi.org/10.1023/A:1001171313493.

——, C. K. Thomas, A. A. Grachev, and P. O. G. Persson, 2018: Near-surface vertical flux divergence in the stable boundary layer. *Bound.-Layer Meteor.*, **169**, 373–393, https://doi.org/10.1007/s10546-018-0379-x.

Maroneze, R., O. C. Acevedo, F. D. Costa, F. S. Puhales, G. Demarco, and L. Mortarini, 2019a: The nocturnal boundary layer transition from weakly to very stable. Part II: Numerical simulation with a second-order model. *Quart. J. Roy. Meteor. Soc.*, **145**, 3593–3608, https://doi.org/10.1002/qj.3643.

——, ——, ——, and J. Sun, 2019b: Simulating the regime transition of the stable boundary layer using different simplified models. *Bound.-Layer Meteor.*, **170**, 305–321, https://doi.org/10.1007/s10546-018-0401-3.

McNider, R. T., D. E. England, M. J. Friedman, and X. Shi, 1995: Predictability of the stable atmospheric boundary layer. *J. Atmos. Sci.*, **52**, 1602–1614, https://doi.org/10.1175/1520-0469(1995)052<1602:POTSAB>2.0.CO;2.

——, and Coauthors, 2012: Response and sensitivity of the nocturnal boundary layer over land to added longwave radiative forcing. *J. Geophys. Res.*, **117**, D14106, https://doi.org/10.1029/2012JD017578.

——, and Coauthors, 2018: Examination of the physical atmosphere in the great lakes region and its potential impact on air quality—Overwater stability and satellite assimilation. *J. Appl. Meteor. Climatol.*, **57**, 2789–2816, https://doi.org/10.1175/JAMC-D-17-0355.1.

Mellor, G. L., and T. Yamada, 1974: A hierarchy of turbulence closure models for planetary boundary layers. *J. Atmos. Sci.*, **31**, 1791–1806, https://doi.org/10.1175/1520-0469(1974)031<1791:AHOTCM>2.0.CO;2.

——, and ——, 1982: Development of a turbulence closure model for geophysical fluid problems. *Rev. Geophys.*, **20**, 851–875, https://doi.org/10.1029/RG020i004p00851.

Nieuwstadt, F. T., 1984: The turbulent structure of the stable, nocturnal boundary layer. *J. Atmos. Sci.*, **41**, 2202–2216, https://doi.org/10.1175/1520-0469(1984)041<2202:TTSOTS>2.0.CO;2.

Poulos, G. S., and S. P. Burns, 2003: An evaluation of bulk Ri-based surface layer flux formulas for stable and very stable conditions with intermittent turbulence. *J. Atmos. Sci.*, **60**, 2523–2537, https://doi.org/10.1175/1520-0469(2003)060<2523:AEOBRS>2.0.CO;2.

Puhales, F. S., O. C. Acevedo, F. D. Costa, L. G. N. Martins, V. Anabor, G. Demarco, and G. A. Degrazia, 2016: Some aspects of the turbulent kinetic energy dissipation rate in the stable boundary layer. *22nd Symp. on Boundary Layer and Turbulence*, Salt Lake City, UT, Amer. Meteor. Soc., 2A.5, https://ams.confex.com/ams/32AgF22BLT3BG/webprogram/Paper295716.html.

ReVelle, D. O., 1993: Chaos and "bursting" in the planetary boundary layer. *J. Appl. Meteor.*, **32**, 1169–1180, https://doi.org/10.1175/1520-0450(1993)032<1169:CAITPB>2.0.CO;2.

Rodrigo, J. S., and P. S. Anderson, 2013: Investigation of the stable atmospheric boundary layer at Halley Antarctica. *Bound.-Layer Meteor.*, **148**, 517–539, https://doi.org/10.1007/s10546-013-9831-0.

Sandu, I., A. Beljaars, P. Bechtold, T. Mauritsen, and G. Balsamo, 2013: Why is it so difficult to represent stably stratified conditions in numerical weather prediction (NWP) models? *Adv. Model. Earth Syst.*, **5**, 117–133, https://doi.org/10.1002/jame.20013.

Savijärvi, H., 2009: Stable boundary layer: Parametrizations for local and larger scales. *Quart. J. Roy. Meteor. Soc.*, **135**, 914–921, https://doi.org/10.1002/qj.423.

Schmengler, M., F. D. Costa, O. C. Acevedo, F. S. Puhales, G. Demarco, L. G. N. Martins, and L. E. Medeiros, 2015: Comparison of mixing length formulations in a single-column model simulation for a very stable site. *Amer. J. Environ. Eng.*, **5**, 106–118, https://doi.org/10.5923/s.ajee.201501.14.

Shi, X., R. T. McNider, M. Singh, D. E. England, M. J. Friedman, W. M. Lapenta, and W. B. Norris, 2005: On the behavior of the stable boundary layer and the role of initial conditions. *Pure Appl. Geophys.*, **162**, 1811–1829, https://doi.org/10.1007/s00024-005-2694-7.

Steeneveld, G., B. Van de Wiel, and A. Holtslag, 2006: Modeling the evolution of the atmospheric boundary layer coupled to the land surface for three contrasting nights in CASES-99. *J. Atmos. Sci.*, **63**, 920–935, https://doi.org/10.1175/JAS3654.1.

——, M. Wokke, C. Groot Zwaaftink, S. Pijlman, B. Heusinkveld, A. Jacobs, and A. Holtslag, 2010: Observations of the radiation divergence in the surface layer and its implication for its parameterization in numerical weather prediction models. *J. Geophys. Res.*, **115**, D06107, https://doi.org/10.1029/2009JD013074.

——, A. Holtslag, R. McNider, and R. Pielke Sr., 2011: Screen level temperature increase due to higher atmospheric carbon dioxide in calm and windy nights revisited. *J. Geophys. Res.*, **116**, D02122, https://doi.org/10.1029/2010JD014612.

Sun, J., L. Mahrt, R. M. Banta, and Y. L. Pichugina, 2012: Turbulence regimes and turbulence intermittency in the stable boundary layer during CASES-99. *J. Atmos. Sci.*, **69**, 338–351, https://doi.org/10.1175/JAS-D-11-082.1.

——, ——, C. Nappo, and D. H. Lenschow, 2015: Wind and temperature oscillations generated by wave–turbulence interactions in the stably stratified boundary layer. *J. Atmos. Sci.*, **72**, 1484–1503, https://doi.org/10.1175/JAS-D-14-0129.1.

Svensson, G., and Coauthors, 2011: Evaluation of the diurnal cycle in the atmospheric boundary layer over land as represented by a variety of single-column models: The second GABLS experiment. *Bound.-Layer Meteor.*, **140**, 177–206, https://doi.org/10.1007/s10546-011-9611-7.

Taylor, P. A., and Y. Delage, 1971: A note on finite-difference schemes for the surface and planetary boundary layers. *Bound.-Layer Meteor.*, **2**, 108–121, https://doi.org/10.1007/BF00718091.

Therry, G., and P. Lacarrère, 1983: Improving the eddy kinetic energy model for planetary boundary layer description. *Bound.-Layer Meteor.*, **25**, 63–88, https://doi.org/10.1007/BF00122098.

Tikhomirov, V. M., 2012: *Mathematics and Mechanics*. Vol. I, *Selected Works of AN Kolmogorov*, Springer Science and Business Media, 551 pp.

van der Linden, S. J., P. Baas, J. Antoon van Hooft, I. G. van Hooijdonk, F. C. Bosveld, and B. J. van de Wiel, 2017: Local characteristics of the nocturnal boundary layer in response to external pressure forcing. *J. Appl. Meteor. Climatol.*, **56**, 3035–3047, https://doi.org/10.1175/JAMC-D-17-0011.1.

Van de Wiel, B., R. Ronda, A. Moene, H. De Bruin, and A. Holtslag, 2002a: Intermittent turbulence and oscillations in the stable boundary layer over land. Part I: A bulk model. *J. Atmos. Sci.*, **59**, 942–958, https://doi.org/10.1175/1520-0469(2002)059<0942:ITAOIT>2.0.CO;2.

——, A. Moene, R. Ronda, H. De Bruin, and A. Holtslag, 2002b: Intermittent turbulence and oscillations in the stable boundary layer over land. Part II: A system dynamics approach. *J. Atmos. Sci.*, **59**, 2567–2581, https://doi.org/10.1175/1520-0469(2002)059<2567:ITAOIT>2.0.CO;2.

——, ——, and H. Jonker, 2012a: The cessation of continuous turbulence as precursor of the very stable nocturnal boundary layer. *J. Atmos. Sci.*, **69**, 3097–3115, https://doi.org/10.1175/JAS-D-12-064.1.

——, ——, ——, P. Baas, S. Basu, J. Donda, J. Sun, and A. Holtslag, 2012b: The minimum wind speed for sustainable turbulence in the nocturnal boundary layer. *J. Atmos. Sci.*, **69**, 3116–3127, https://doi.org/10.1175/JAS-D-12-0107.1.

——, and Coauthors, 2017: Regime transitions in near-surface temperature inversions: A conceptual model. *J. Atmos. Sci.*, **74**, 1057–1073, https://doi.org/10.1175/JAS-D-16-0180.1.

van Hooijdonk, I. G., J. M. Donda, H. J. Clercx, F. C. Bosveld, and B. J. van de Wiel, 2015: Shear capacity as prognostic for nocturnal boundary layer regimes. *J. Atmos. Sci.*, **72**, 1518–1532, https://doi.org/10.1175/JAS-D-14-0140.1.

Vignon, E., and Coauthors, 2017: Stable boundary-layer regimes at Dome C, Antarctica: Observation and analysis. *Quart. J. Roy. Meteor. Soc.*, **143**, 1241–1253, https://doi.org/10.1002/qj.2998.

Weng, W., and P. A. Taylor, 2003: On modelling the one-dimensional atmospheric boundary layer. *Bound.-Layer Meteor.*, **107**, 371–400, https://doi.org/10.1023/A:1022126511654.

——, and ——, 2006: Modelling the one-dimensional stable boundary layer with an E–l turbulence closure scheme. *Bound.-Layer Meteor.*, **118**, 305–323, https://doi.org/10.1007/s10546-005-2774-3.

Zhang, D., and R. A. Anthes, 1982: A high-resolution model of the planetary boundary layer—Sensitivity tests and comparisons with SESAME-79 data. *J. Appl. Meteor.*, **21**, 1594–1609, https://doi.org/10.1175/1520-0450(1982)021<1594:AHRMOT>2.0.CO;2.

Zilitinkevich, S., T. Elperin, N. Kleeorin, I. Rogachevskii, and I. Esau, 2013: A hierarchy of energy-and flux-budget (EFB) turbulence closure models for stably-stratified geophysical flows. *Bound.-Layer Meteor.*, **146**, 341–373, https://doi.org/10.1007/s10546-012-9768-8.